Research Article | Vol. 11, No. 2 / February 2024 / *Optica* 1

OPTICA

Quartz as an accurate high-field low-cost THz helicity detector

Maximilian Frenzel,[1] Joanna M. Urban,[1] Leona Nest,[1] Tobias Kampfrath,[1,2] Michael S. Spencer,[1] and Sebastian F. Maehrlein[1,*]

[1]*Department of Physical Chemistry, Fritz Haber Institute of the Max Planck Society, 14195 Berlin, Germany*
[2]*Department of Physics, Freie Universität Berlin, 14195 Berlin, Germany*
**maehrlein@fhi-berlin.mpg.de*

Received 20 December 2023; revised 2 February 2024; accepted 2 February 2024; published 0 MONTH 0000

Emerging concepts employing angular momentum of THz light for ultrafast material control rely on the measurement of undistorted intense THz fields and on the precise knowledge about sophisticated THz helicity states. Here, we establish z-cut α-quartz as a precise electro-optic THz detector for full amplitude, phase, and polarization measurement of highly intense THz fields, all at a fraction of costs of conventional THz detectors. We experimentally determine its detector response function, in excellent agreement with our modeling. Thereupon, we develop a swift and reliable protocol to precisely measure arbitrary THz polarization and helicity states. This two-dimensional electro-optic sampling in α-quartz fosters rapid and cost-efficient THz time-domain ellipsometry and enables the characterization of polarization-tailored fields for driving chiral or other helicity-sensitive quasi-particles and topologies.

https://doi.org/10.1364/OPTICA.515909

1. INTRODUCTION

THz sources with peak field strengths in the ~1 MV/cm regime based on optical rectification in $LiNbO_3$ [1] and organic crystals [2,3], difference frequency generation [4], large-area spintronic emitters [5], and large-scale accelerator facilities [6] are becoming more widely accessible. This development has enabled the selective drive of low-energy excitations such as phonons [7,8], magnons [9], or other quasi-particles, thereby allowing for ultrafast control over material properties and nonequilibrium material design toward light-induced superconductivity [10], ferroelectricity [11], ferromagnetism [12], and spin-dynamics [9,13]. However, despite large improvements in THz generation, the detection of intense single-cycle THz fields without distortions has remained challenging [14,15].

Field-resolved THz detection provides precise frequency resolution of the amplitude and phase of the light field. This feature is crucial for, e.g., THz time-domain spectroscopy (THz-TDS) [16], THz emission spectroscopy [15], and state-of-the-art experiments involving THz high-harmonic generation in topological insulators [17], graphene [18], or superconducting cuprates [19]. Moreover, emerging field-driven effects, e.g., for ultrafast control of topological [20] or chiral [21–23] material properties, are inherently sensitive to the carrier-envelope phase (CEP) and polarization (incl. helicity) of the driving THz pulse. Full vectorial THz-field characterization is required for the precise detection of arbitrary THz polarization states. This information also constitutes the basis for THz time-domain ellipsometry, which allows for the characterization of tensorial dielectric properties in opaque [24], anisotropic materials [25], and transient metamaterials [26], where traditional THz-TDS faces limitations. Another application is THz circular-dichroism spectroscopy, which has been applied in chiral nanostructures and molecular assemblies [27], thermoelectric solids [28], or bio-relevant systems such as DNA [29] and living cancer cells [30]. However, partly due to the difficulty of precise polarization-resolved THz detection, THz time-domain ellipsometry and circular-dichroism spectroscopy have not been widely adopted yet.

The common technique to detect phase-stable THz fields is electro-optic sampling (EOS) [31]. Here, the incident THz pulse induces a change in birefringence proportional to the THz electric field in a nonlinear crystal like ZnTe [32] or GaP [33], which can be stroboscopically sampled by a visible (VIS) or near-infrared (NIR) sampling pulse as a function of time delay t. However, the measured instantaneous signal $S(t)$ is, in general, not simply proportional to the instantaneous field $E(t)$. Within linear response theory and in frequency space, a response function h connects S and E at THz frequencies $\Omega/2\pi$ via $S(\Omega) = h(\Omega)E(\Omega)$ and captures the frequency dependence of the nonlinear susceptibility $\chi^{(2)}$, which can be strongly modulated by phonons [31], and nonlocal effects, such as phase mismatch between THz- and sampling pulse [34,35].

For (110)-oriented zincblende-type electro-optic crystals such as ZnTe (110), resolving the polarization state of THz pulses typically requires rotation of the detector crystal and sampling pulse polarization [36]. Unfortunately, such measurements can be easily polluted by inhomogeneities of the detector crystal, birefringence effects, or inaccurate rotation axes. On the other hand, (111)-oriented zincblende crystals enable polarization state retrieval by simply modulating the sampling pulse polarization by using, e.g., a photoelastic modulator [37] or employing a dual-detection scheme based on two balanced detections [38]. Nonetheless, the specific detector requirements and additional experimental effort have limited the application of polarization-resolved EOS so far.

Extending these concepts to highly intense THz fields poses extra challenges, since they can lead to distorted signals in conventional EOS crystals, such as ZnTe or GaP, which include over-rotation [14] or higher-order nonlinearities such as the THz Kerr effect [39,40] (see Supplement 1, Fig. S4). This aspect means that the amplitude and phase of intense THz fields cannot be reliably extracted within the linear response. Likewise, attenuating the THz fields by using, e.g., wiregrid polarizers or filters such as silicon wafers [1], might induce additional spectral distortions [41] and Fabry–Perot resonances.

Here, we focus on z-cut α-quartz, which is a widely used substrate material for THz-TDS due to its high THz transparency [16] and in-plane optical isotropy. It recently attracted attention as a promising nonlinear THz material [42], i.e., as a broadband THz emitter via optical rectification [43] or as a THz detector via EOS [44]. Its large bandgap and optical transparency allow for a broad dynamic range and high damage threshold. Moreover, α-quartz is widely available at 2 orders of magnitude lower cost than typical EOS crystals. However, there are significant drawbacks that prevented the reliable use of quartz for THz detection so far. In particular, the response function h has been unknown, and its peculiar thickness dependence lead to the open question regarding bulk versus surface $\chi^{(2)}$ contributions [44]. Additionally, the polarization-sensitivity has remained mostly unexplored.

In this work, we experimentally measure the quartz response function and model it predominantly based on known literature values. We show that arbitrary THz polarization states can be measured by a simple and time-efficient method utilizing only two EOS measurements with different sampling pulse polarizations. The latter is achieved by a simple rotation of a half-wave plate (HWP) in the VIS spectral range. As a textbook example for time-domain ellipsometry, we determine the birefringence of y-cut quartz as commonly used for commercial THz wave plates. We find that the transmitted single-cycle pulses exhibit complex polarization states in the highly polychromatic regime [45], which cannot be described by a single polarization ellipse, Jones vector, or set of Stokes parameters. Our study establishes z-cut α-quartz as a reference detector for amplitude, phase, and arbitrary polarization states of THz fields exceeding 100 kV/cm, fostering cost-efficient high-field THz time-domain ellipsometry and tailoring helical THz driving fields for ultrafast material control.

2. EXPERIMENTAL SETUP

Intense single-cycle THz fields [1.3 THz center frequency, 1.5 THz full width at half-maximum (FWHM)] with peak fields exceeding 1 MV/cm are generated by tilted-pulse-front optical rectification in $LiNbO_3$ [1]. The THz field strengths or its linear polarization angle ψ relative to the vertical direction in the lab frame are altered using a THz polarizer pair, P1 and P2 in Fig. 1(a). The THz field-induced birefringence in the EOS crystal is probed by synchronized VIS sampling pulses (800 nm center wavelength, ~20 fs duration) using a balanced detection scheme. The sampling pulse's incident linear polarization can be set to arbitrary angles θ by a broadband VIS HWP. We measure EOS in a ZnTe (110) crystal (10 µm thickness) and various z-cut α-quartz plates with thicknesses of 35, 50, 70, and 150 µm as a function of sampling pulse polarization θ, THz polarization ψ, and the crystal's azimuthal angle ϕ at normal incidence (see Fig. 1(a) and Supplement 1, Section 1 for more information). Finally, we also trace the THz field after collimated transmission through highly birefringent y-cut α-quartz (700 µm thickness), which corresponds to a commercial quarter-wave plate (QWP) at ~2.2 THz.

3. RESULTS

A. Electro-Optic Response Function

We first confirm the linear response function relation. Figure 1(b) shows the measured THz-induced birefringence signals $S(t)/S_{\max}$ in 50 µm quartz for different THz peak fields. The induced birefringence scales linearly with the THz electric field strength [see inset of Fig. 1(b)], confirming a linear electro-optic effect as recently observed by Balos *et al.* [44]. The normalized time- and frequency-domain shapes [see Figs. 1(b) and 1(c)] do not change substantially for different THz fluences, ruling out over-rotation effects and demonstrating only small spectral deviations (e.g., <1.5 THz). Recently unveiled higher-order nonlinearities [42] amount to maximum 1% for THz fields of the order of 1 MV/cm (see Supplement 1, Section 8). This finding confirms that quartz can reliably sample THz electric fields ≥100 kV/cm within the linear-response regime (see Supplement 1, Fig. S4 for comparison with ZnTe).

To experimentally extract the linear response function of 50 µm quartz, we compare the quartz EOS signal S_{Q} with the signal S_{ZnTe} from 10 µm ZnTe, whose response function h_{ZnTe} is known [34] [see Fig. 2(a)]. To avoid nonlinear distortions, the THz power for ZnTe was attenuated by the THz polarizer pair by a factor of ~40. We Fourier transform these traces and extract the quartz response using $h_{\mathrm{Q}} = h_{\mathrm{ZnTe}}(S_{\mathrm{Q}}/S_{\mathrm{ZnTe}})$ in the frequency domain. The amplitude and phase of h_{Q} are shown as blue dots in Figs. 2(b) and 2(d), respectively, demonstrating that the quartz response covers the full 0.1–4 THz bandwidth of the $LiNbO_3$ source without gaps. However, it contains a substantial frequency dependence in the form of modulations with a frequency spacing of ~1.4 THz as well as an enhancement at low frequencies <0.9 THz and at around 3.9 THz.

B. Modeling

To understand the experimental response function $h_{\mathrm{Q,exp}}(\Omega)$ of 50 µm quartz, we model the response h_{calc} as function of THz frequency Ω by extending the formalism of Ref. [34] and use

$$h(\Omega) = \chi^{(2)}_{\mathrm{eff}}(\Omega) t_{\mathrm{F}}(\Omega) \int_{\omega>\Omega} \mathrm{d}\omega \frac{\omega^2}{c^2 k(\omega)} T_{\mathrm{s}}(\omega, \Omega) E^*_{\mathrm{s}}(\omega) \times E_{\mathrm{s}}(\omega - \Omega) G(\omega, \Omega), \quad (1)$$

where $h_{\mathrm{calc}}(\Omega) = [h(\Omega) + h^*(-\Omega)]/(I_1 + I_2)$ and $I_1 + I_2 = \int \mathrm{d}\omega\, T_{\mathrm{s}}(\omega, \Omega = 0) E^*_{\mathrm{s}}(\omega) E_{\mathrm{s}}(\omega)$. Here, E_{s} is the incident sampling pulse with optical frequency $\omega/2\pi$ and wavenumber $k(\omega) = n(\omega)\omega/c$, where $n(\omega)$ is the corresponding refractive index. $T_{\mathrm{s}}(\omega, \Omega)$ accounts for the sampling pulse transmission

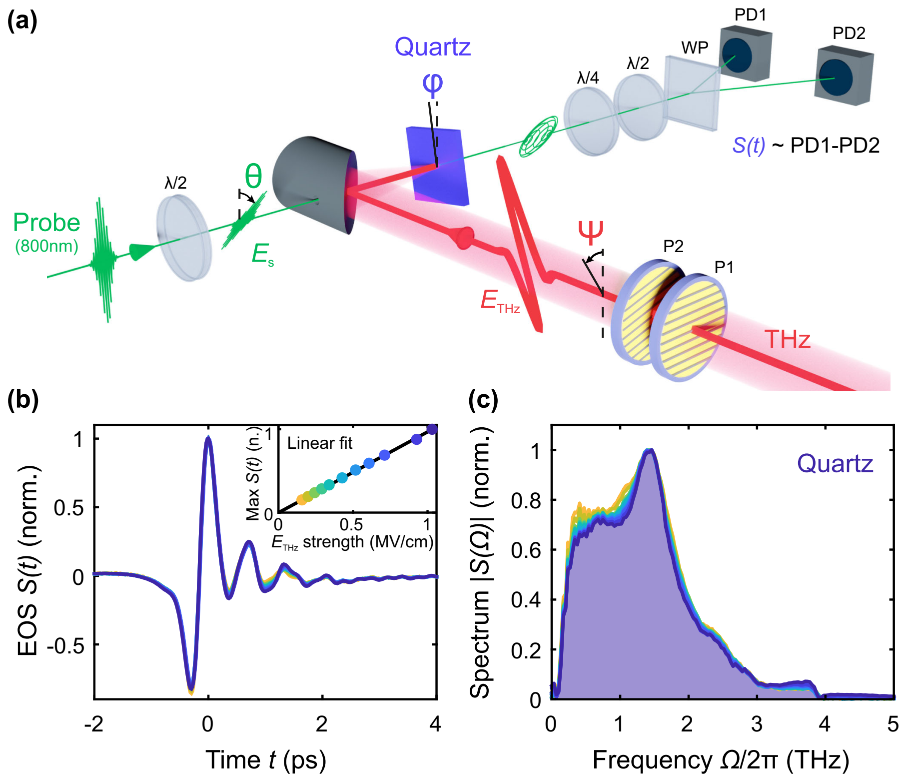

Fig. 1. Electro-optic sampling in quartz and its THz fluence dependence. (a) Experimental setup: THz pulses are generated via optical rectification (OR) in $LiNbO_3$. The THz pulse induces a refractive index change in quartz, leading the sampling pulse to acquire ellipticity. This ellipticity is read out as signal $S(t)$ as a function of time delay t in a balanced detection scheme. S is related to the incident THz field E_{THz} via the complex detector response function h_Q. (b) EOS in quartz (z-cut, 50 μm thickness) for different THz fluences, normalized to the $t = 0$ peak EOS values. Inset: linear dependence of peak $S(t)$ on peak E_{THz}. (c) $S(\Omega)$ amplitude spectrum via Fourier transform of EOS signals $S(t)$ in (b) normalized to spectral peak amplitude.

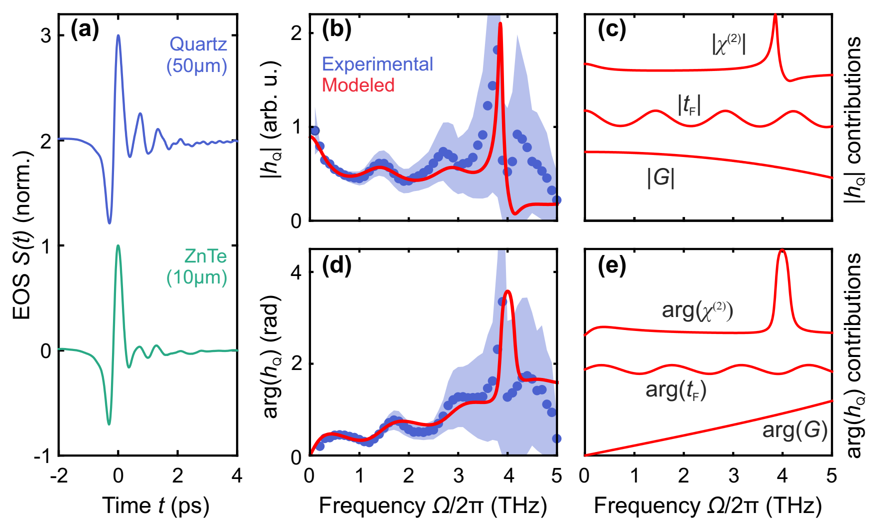

Fig. 2. Experimentally measured and calculated detector response. (a) Normalized EOS signal $S(t)$ in quartz (50 μm thickness) and ZnTe (10 μm thickness). (b), (d) Complex quartz response function h_Q for 50 μm is experimentally extracted using known ZnTe response and $h_Q = (S_{ZnTe}\, h_{ZnTe})/S_Q$ (blue) and modeled using Eq. (1) (red) in amplitude and phase. (c), (e) Modeled $\chi^{(2)}$, transmitted field coefficient t_F, and phase-matching factor G in amplitude and phase, showing how these factors contribute to the quartz response function.

$T_s(\omega, \Omega) = t_{12}^*(\omega) t_{21}^*(\omega) t_{12}(\omega - \Omega) t_{21}(\omega - \Omega)$, where $t_{12}(\omega)$ and $t_{21}(\omega)$ are the Fresnel transmission coefficients for propagating from air into quartz and quartz into air, respectively. $\chi_{\text{eff}}^{(2)}(\Omega) = \chi_{\text{eff}}^{(2)}(\omega_c, \Omega)$ is the effective nonlinear susceptibility of the detection crystal under the assumption that $\chi_{\text{eff}}^{(2)}(\omega - \Omega, \Omega) \approx \chi_{\text{eff}}^{(2)}(\omega_c, \Omega)$, where ω_c is the sampling-pulse center frequency. The field transmission coefficient $t_F(\Omega)$ accounts for the transmitted THz field including its multiple reflections (see Supplement 1, Section 2 for more information). The phase-matching factor, $G(\omega, \Omega) = [\exp(i\Delta k(\omega, \Omega)d) - 1]/i\Delta k(\omega, \Omega)$, between THz and sampling pulse includes $\Delta k(\omega, \Omega) = k(\omega - \Omega) + k(\Omega) - k(\omega)$ and the sample thickness d.

To calculate h_Q, we use the known quartz refractive indices in the THz [16] and optical regions [46]. However, the nonlinear susceptibility $\chi^{(2)}(\Omega)$ is not known and we therefore model it by

$$\chi^{(2)}_{\mathrm{eff}}(\Omega) = \chi^{(2)}_e \left[1 + B\left(1 - i\Omega\tau_{\mathrm{D}}\right)^{-1} + C\left(1 - \frac{\Omega^2}{\Omega^2_{\mathrm{TO}}} - \frac{i\Omega\Gamma}{\Omega^2_{\mathrm{TO}}}\right)^{-1} \right], \tag{2}$$

where $\chi^{(2)}_e$ is the pure electronic susceptibility. The last term corresponds to the ionic contribution with ω_{TO} being the frequency, and Γ being the damping of the respective transverse-optical (TO) phonon, while the Faust–Henry coefficient C defines the ratio between the lattice-induced and electronic contributions [31,47]. We take the phonon parameters $\Omega_{\mathrm{TO}}/(2\pi) = 3.9$ THz and $\Gamma/(2\pi) = 0.09$ THz from Davies *et al.* [16] and find $C = 0.15$ to provide good agreement with our experimental values [see red curves in Figs. 2(b) and 2(d)]. We assume that the striking low-frequency enhancement of $h_Q(\Omega)$ [see Fig. 2(b)] arises from $\chi^{(2)}$ and model it by a phenomenological Debye-type relaxation contribution B with characteristic time scale τ_{D} [second term in Eq. (2)]. Choosing $B = 0.7$ and $\tau_{\mathrm{D}} = 0.5$ ps provides nearly perfect agreement with the 0.1–0.9 THz range in $h_{Q,\mathrm{exp}}$. We will discuss possible physical origins of such a contribution below. Thus, by analytic modeling, we find dominating contributions by the phase-matching factor G, the field transmission coeffient t_{F}, and the nonlinear susceptibility $\chi^{(2)}$, disentangled in Figs. 2(c) and 2(e).

We apply the response function to calculate the exact THz electric field (red) from the quantitative EOS signal in 50 μm quartz (blue) in Figs. 3(a) and 3(b) in the time and frequency domains, respectively. To determine the absolute field strength, we use the measured THz pulse energy and focal size (see Supplement 1, Section 3). We obtain a peak field strength of 1.04 MV/cm. We can therefore estimate the effective electro-optic coefficient r_{eff}, which equals the r_{11} tensor component, of z-cut quartz to be 0.1 pm/V (see Supplement 1, Section 4). This value agrees well with previous reports of r_{11} at optical frequencies ranging between 0.1 and 0.3 pm/V in z-cut quartz [48,49].

C. Thickness Dependence and Origin of Nonlinearity

The response function also depends on the crystal thickness, which typically presents a trade-off between sensitivity and bandwidth. Figure 3(c) shows the measured dependence of the maximum EOS signal on the quartz crystal thickness between 35 and 150 μm (blue dots), which clearly deviates from an ideal phase-matched behavior, i.e., a linear scaling with the crystal thickness. We also observe a noticeable thickness dependence of the time-domain EOS shapes in Fig. 3(d), even clearer in the spectral bandwidth in Fig. 3(e). Figure 3(f) displays the calculated response function for each thickness in amplitude (red) and phase (gray), which explains the measured features. For instance, the effective bandwidth is significantly lower for 150 μm quartz due to the zero in the phase-matching factor $G(\Omega, \omega)$, while the thickness-dependent frequency spacing of the modulations generally arise from Fabry–Perot fringes in the field transmission coefficient $t_{\mathrm{F}}(\Omega)$. The calculated response function, thus, also explains the experimentally observed EOS thickness dependence in Fig. 3(c) (red line), mainly by the phase mismatch $G(\Omega, \omega)$ of THz and sampling pulse.

The first report of EOS in quartz suggested a strong surface $\chi^{(2)}$ contribution [44]. Indeed, the surface and bulk $\chi^{(2)}$ have a similar order of magnitude [50]. As the surface contribution originates from a depth of ∼1 nm (Ref. [50]), its contribution will be small in comparison to the bulk contribution for a quartz crystal with a thickness >10 μm. The response functions presented here [Figs. 2(b), 2(d), and 3(f)] strongly indicate a pure bulk $\chi^{(2)}$ effect and provide a reasonable estimate of r_{11}, both sufficient to explain the experimental observations.

We suggest the low-frequency (0.1–0.9 THz) enhancement in $\chi^{(2)}$ to be caused by disorder. In fact, the frequency region 0.1–1.2 THz of fused silica and other glasses is often associated with the so-called Boson-peak behavior corresponding to low-frequency vibrational modes [51,52]. Its nature and origin remain debated, but it is known to affect the Raman, neutron, and linear dielectric responses of quartz and related glasses [51–53]. Our finding, thus, motivates further research into the nonlinear susceptibility in the sub-0.9 THz region. In addition, there is considerable variability

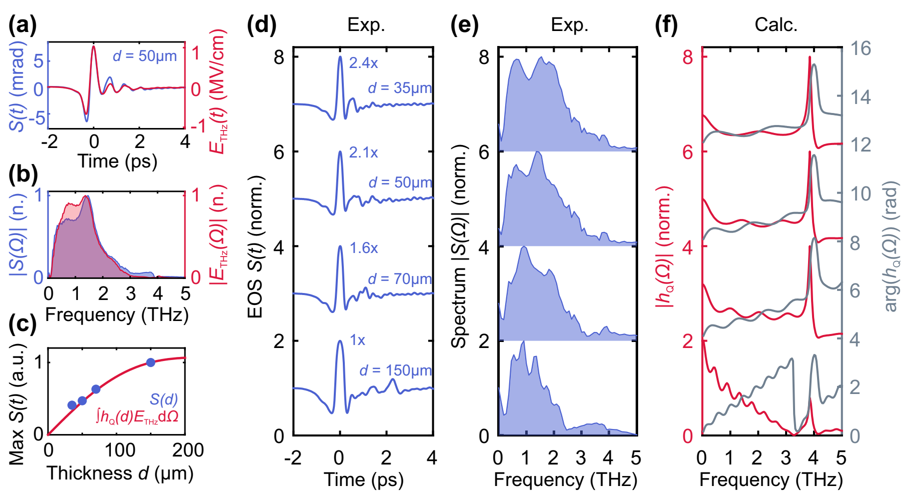

Fig. 3. Thickness dependence and extracted THz electric fields. (a) Absolute THz electric field E_{THz} extracted by applying the response function h_Q to the measured EOS signal S with 50 μm quartz and (b) corresponding Fourier amplitude spectrum. (c) Maximum EOS signal $S(t)$ as a function of quartz thickness (blue markers) and calculated quartz response (red curve). (d) EOS signal for four different quartz thicknesses below 150 μm with (e) respective Fourier amplitude spectra. (f) Modulus and phase of calculated detector response h_Q of quartz for the respective thicknesses. The small oscillatory variations below 4 THz are Fabry–Perot resonances. The zero in (e) for 150 μm is dictated by the phase-matching factor G. The peak at 3.9 THz stems from the phonon contribution to $\chi^{(2)}$.

of the reported values for the 3.9 THz phonon damping parameter $\Gamma/2\pi$ between 0.09 THz (Ref. [16]) and 0.39 THz (Ref. [53]). While we found that the measured quartz responses are homogeneous across the individual samples, the variation of literature values indicates that the $\chi^{(2)}$ model parameters could be highly sensitive to the overall sample quality.

D. Polarization-Resolved EOS

So far, we have treated both h_Q and E_{THz} as scalars and only considered the specific case in which the THz-pulse and sampling-pulse polarizations are parallel and the quartz azimuthal angle is optimized for maximum $S(t)$, i.e., oriented parallel to one of the in-plane crystalline axes. However, the THz electric field is a vectorial observable and can have an arbitrary (and thus even helical) polarization state and h_Q is generally dependent on the azimuthal angle ϕ and sampling pulse polarization θ. We can assume the same frequency-dependence of the allowed $\chi^{(2)}$ tensor elements and any corresponding linear combination of them, because of the in-plane symmetry of the 3.9 THz phonon. Since the other quantities in Eq. (1), such as t_F or G, refer to linear optical properties, they are also in-plane isotropic in z-cut quartz. We can, therefore, assume the same frequency evolution of the response function for all ϕ and θ, but the absolute sensitivity will be rescaled by the global symmetry of $\chi_e^{(2)}(\phi, \theta)$, which ultimately allows for polarization-sensitive THz EOS.

To explore the sensitivity of 50 μm quartz to different THz field polarization components, Fig. 4(a) shows the measured peak EOS signal S (blue dots) as a function of quartz azimuthal angle ϕ for three different probe polarizations $\theta = 0°, 45°, 90°$ with respect to the THz field ($\psi = 0°$, linearly polarized along the y axis). For each probe polarization, rebalancing of the detection wave plates is required, which can be simply automated by using motorized rotation stages. Each azimuthal dependence $S(\phi)$ exhibits a perfect three-fold symmetry in agreement with the first reported quartz EOS [44]. We therefore calculate the expected dependence of $S(\psi, \theta)$ for a THz field $\mathbf{E}_{THz}$ linearly polarized at an arbitrary angle ψ, and sampling field $\mathbf{E}_s$ linearly polarized at angle θ in the x–y plane [see Fig. 1(a)]. We use the second-order nonlinear polarization $P_i^{(2)} = \epsilon_0 \chi_{ijk}^{(2)} E_j^{THz} E_k^s$, which we can rewrite using the nonlinear susceptibility tensor in contracted notation d_{il} with only nonzero d_{11} and d_{14} terms due to quartz's D_3 point group, evaluated for the z-cut plane [54] (see Supplement 1, Section 5). The blue line in Fig. 4(a) shows the expected sensitivity for a vertically polarized THz field E_y^{THz} (i.e., $\psi = 0°$), in perfect agreement with the measured azimuthal dependence. The expected peak signal for a horizontally polarized THz field E_x^{THz} (i.e., $\psi = 90°$), shown as a red line, features the same three-fold symmetry but shifted by 30°. These opposite EOS sensitivities for the x- and y-projections of the THz field allow for a full THz polarization determination by simply measuring EOS for two different sampling pulse polarizations, e.g., $\theta = 0°$ for obtaining E_y^{THz} and $\theta = 45°$ for obtaining E_x^{THz} at azimuth $\phi = 0$ [see square markers in Fig. 4(a)].

To prove this concept, we rotate the linear polarization of the THz pulse by setting polarizer P1 to 45° and scanning P2 by angle ψ. Next, we measure $S(t)$ for sampling pulse polarization $\theta = 0°$ (S_0) and 45° (S_{45}) for a set of THz polarizer angles ψ. Figure 4(b) shows that $\arctan(S_{45}/S_0)$ is identical to the THz polarizer angle ψ and, thus, precisely measures the THz polarization by only two EOS measurements at different sampling pulse polarizations. After applying the calculated response function h_Q to S_0 and S_{45}, the full vectorial THz field $E_{THz}(t)$ can be extracted as shown in the 2D-EOS traces for selected ψ between 0° and 90° in Fig. 4(c). We note that the perfect three-fold symmetry is not found in the common ZnTe (110) or GaP (110) EOS crystals, where this convenient procedure cannot be used and the crystal has to be rotated instead [38].

E. Broadband THz Helicity Measurement

For driving chiral or, generally, helicity-dependent excitations, e.g., for ultrafast control of phonon angular momentum [22,23,55] or topology modulation [20], CEP-stable table-top THz sources are beneficial due to their inherent synchronization with sub-cycle probing pulses. Nevertheless, to reach the required peak fields, the energy has to be squeezed into few- or single-cycle pulses at low repetition rates. With the general lack of broadband THz wave plates, this leads to complicated polarization states when aiming for THz pulses with specific helicities. In contrast to conventional multi-cycle optical light, helical few- or single-cycle THz pulses are highly polychromatic and, generally, cannot be described by a single polarization state, i.e., neither by a pair of ellipticity angles (ϑ, η) nor by one fixed Jones or Stokes vector [45]. Instead,

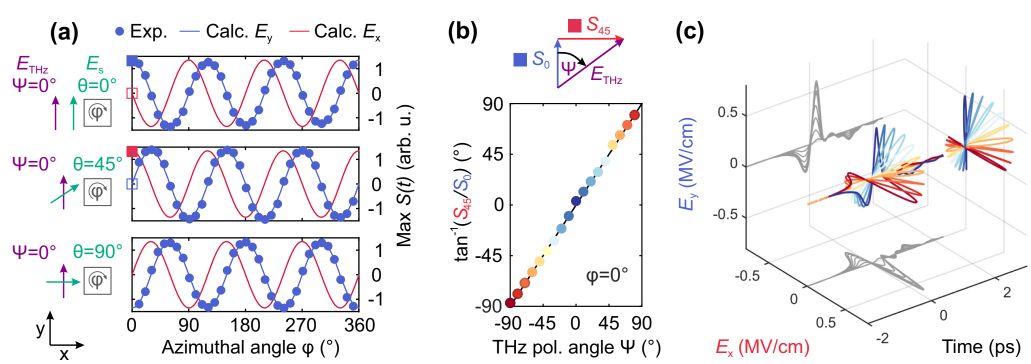

Fig. 4. Polarization and azimuthal angle dependence for 2D-EOS. (a) Measured azimuthal angle ϕ dependence of maximum quartz $S(t)$ for different sampling pulse polarizations (θ) with THz pulse polarized along y (blue dots). Blue and red lines are the calculated azimuthal angle dependence for the respective sampling pulse polarizations and THz polarized along y (blue line) and x (red line). (b) The arctan of the peak EOS signals measured at $\theta = 45°$ (S_{45}) and $\theta = 0°$ (S_0) perfectly matches the THz polarizer angle ψ, demonstrating that the full THz polarization state can be extracted by measuring $S_0(t)$ and $S_{45}(t)$. (c) 2D-EOS: $E_x^{THz}(t)$ and $E_y^{THz}(t)$ for selected ψ between 0° and 90°, which were extracted from $S_{45}(t)$ and $S_0(t)$ by applying the quartz response function h_Q.

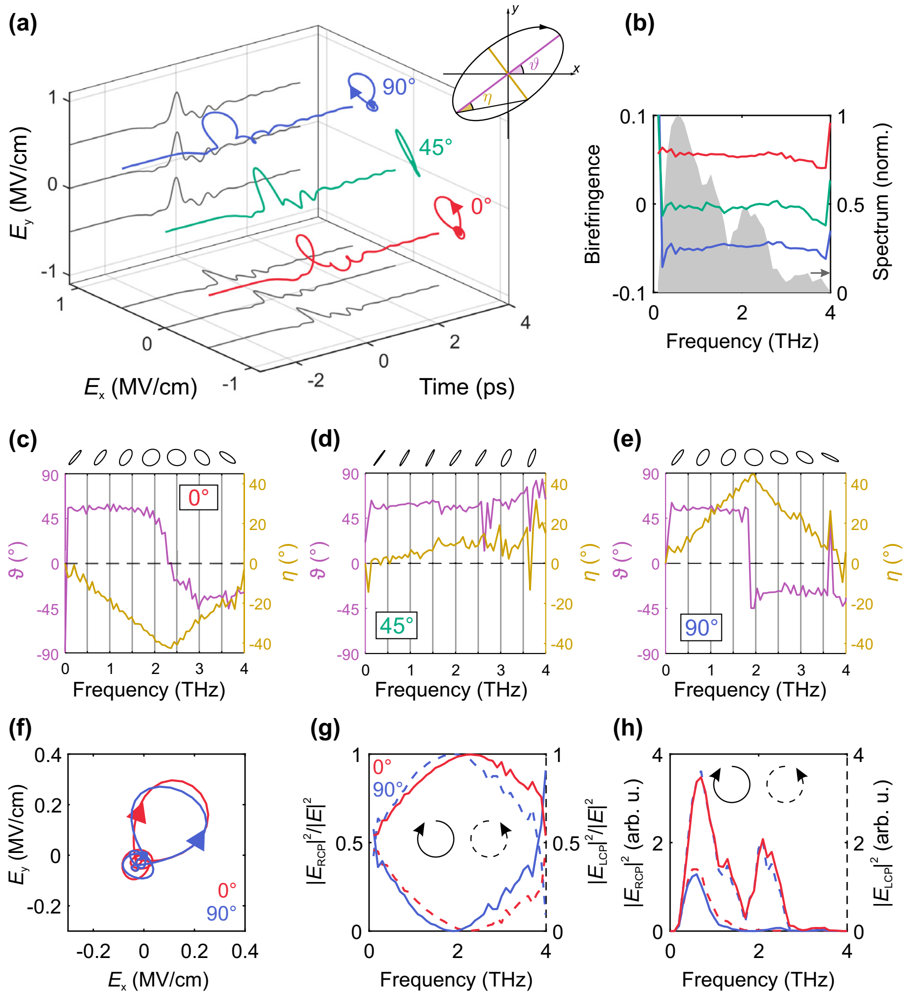

Fig. 5. Detection of arbitrary THz polarization states and their helicity. (a) 2D-EOS of the THz electric field transmitted through a 0.7 mm y-cut quartz plate for three different y-cut quartz orientations, detected in 50 µm z-cut quartz. The y-cut quartz plate was aligned with one of its facets parallel to the y-axis (corresponds to 0°). The incident THz field was linearly polarized at 45°. (b) Extracted birefringence for the three different y-cut quartz azimuthal angles, demonstrating that the THz field experiences the largest birefringence for 0° and 90° quartz-plate orientations. (c)–(e) Corresponding frequency-resolved THz polarization states expressed in polarization ellipse rotation $\vartheta(\Omega)$ and ellipticity $\eta(\Omega)$ for 0°, 45°, and 90° y-cut plate azimuthal angle, respectively. (f) Projection of $E_x^{\mathrm{THz}}(t)$ and $E_y^{\mathrm{THz}}(t)$ into the $(E_x^{\mathrm{THz}}, E_y^{\mathrm{THz}})$ plane for 0° and 90° y-cut plate azimuthal angles, unveiling the different, but not exactly opposite, helicity states. (g) Corresponding LCP and RCP intensity spectra normalized for every frequency Ω to $|E^{\mathrm{THz}}(\Omega)|^2$ and (h) corresponding absolute intensities.

the polarization state must be generally described as an evolution in frequency space or, equivalently, by the full temporal trajectory of the light's electric field vector $\mathbf{E}_{\mathrm{THz}}(t)$.

To demonstrate the complete detection of arbitrary polarization states in quartz, in particular for complicated helical fields, we characterize the polarization state of single-cycle THz pulses after passing through a birefringent y-cut quartz plate (see Supplement 1, Fig. S3), which is nearly identical to commercially available THz wave plates. Figure 5(a) shows the transmitted electric field of a collimated THz beam ($\psi = 45°$) through 0.7 mm crystalline y-cut quartz for three different crystal orientations, which is detected in 50 µm z-cut quartz. The transmitted THz polarizations for 0° and 90° orientations appear highly elliptical, which is when the incident THz pulse polarization is at 45° to the in-plane crystal axes and therefore experiences maximum birefringence. This form of time-domain ellipsometry permits the direct measurement of the birefringence $\Delta n(\Omega)$ using $\arg(E_x^{\mathrm{THz}}) - \arg(E_y^{\mathrm{THz}}) = \Delta n \Omega d/c$, as shown in Fig. 5(b). We find an approximately constant $\Delta n(\Omega)$ of about 0.05 at 0.4–3.5 THz, in good agreement with literature values [53,56].

As seen from Fig. 5(a), the transmitted THz polarization is neither a simple polarization ellipse nor purely left- or right-handed circularly polarized. Its sophisticated electric-field trajectory can be described by a frequency-dependent rotation $\vartheta(\Omega)$ and ellipticity $\eta(\Omega)$ [see inset in Fig. 5(a)], or any other ellipsometric set of parameters as a function of frequency. Figures 5(c)–5(e) show $\vartheta(\Omega)$ and $\eta(\Omega)$ for 0°, 45°, and 90° orientations of the y-cut quartz plate, respectively. For 0° and 90° orientations [see Figs. 5(c) and 5(e)], the THz pulse acquires a maximum of frequency-dependent ellipticity $\Delta n \Omega d/c$. Since $\Delta n(\Omega)$ is roughly constant, the transmitted THz pulses for 0° and 90° orientations are, respectively, perfectly right- and left-handed circularly polarized only at frequency $c/(4\Delta n d) \approx 2.37$ THz and 1.96 THz, where η reaches $-45°$ and 45°. In other words, the y-cut quartz plate acts as a THz QWP for only a very narrow frequency range and leads to drastically different polarization states for all other frequency components within the THz pulse [see top row of Figs. 5(c) and 5(e)]. In contrast, the incident THz pulse acquires a small ellipticity for the 45° orientation [see Fig. 5(d)] only at higher frequencies, which are more sensitive to a small Δn.

Usually, broadband QWPs create opposite helicities for ±45° rotation. This behavior is evidently not the case here, as the two $\mathbf{E}(t)$ trajectories in Fig. 5(f) are not perfectly opposite. Figures 5(g) and 5(h) depict the full frequency-dependent right-handed (E_{RCP}) and left-handed (E_{LCP}) circularly polarized intensity components for the 0° (red) and 90° (blue) orientations, normalized for every frequency component [see Fig. 5(g), and Supplement 1, Section 6] and as absolute intensity spectra [see Fig. 5(h)]. Figure 5(g) highlights that the helicity changes quite drastically across the single THz pulse spectrum and that a circular polarization is achieved at slightly different frequencies for opposite QWP angles (0° versus 90°), in agreement with the ellipticity parameters $\eta(\Omega)$ in Figs. 5(c) and 5(e). This difference cannot be explained by the optical activity of the z-cut quartz detector, since optical activity only affects the measurement of the polarization ellipse rotation $\vartheta(\Omega)$ but not ellipticity $\eta(\Omega)$, and is negligible for 50 µm thin quartz plates [57]. However, the difference can be related to a slightly tilted axis of rotation with respect to the quartz plate's y axis or imperfect linear polarization of the THz field entering the y-cut plate. These aspects highlight the challenges of helicity-dependent measurements in the THz spectral range.

4. DISCUSSION

We now discuss the detector performance of α-quartz in more detail. The found electro-optic coefficient r_{11} of 0.1 pm/V is about an order of magnitude smaller than $r_{41} = 4$ pm/V of ZnTe [32] and 1.6 pm/V of GaP [33], thereby moving nonlinear EOS responses to much higher THz field amplitudes in quartz (see high-field EOS in ZnTe in Supplement 1, Fig. S4), while maintaining sensitivity for fields down to a few kV/cm (see Supplement 1, Section 9). Since we find a pure bulk $\chi^{(2)}$ effect, the phase-matching term G governs the trade-off between detection sensitivity and bandwidth. The effective detector bandwidth is, thus, limited by the first zero in G [Fig. 3(f)], giving a cutoff frequency $\nu_{\mathrm{cutoff}} = c/[(n_{\mathrm{THz}} - n_{\mathrm{s}}^{(\mathrm{g})})d] = 1/(\mathrm{GVM} \cdot d)$. The group-velocity mismatch (GVM) in quartz is about 1.8 ps/mm (assuming $n_{\mathrm{THz}}(1\,\mathrm{THz}) = 2.09$ and group index $n_{\mathrm{s}}^{(\mathrm{g})}(800\,\mathrm{nm}) = 1.55$), which is only slightly larger than in ZnTe (1.1 ps/mm) [32] and GaP (1.2 ps/mm) [33]. A full comparison of r_{eff} and GVM between quartz and the widely used EOS crystals ZnTe and GaP is shown in Supplement 1, Section 7. Therefore, to sample the whole THz spectrum of typical high-field THz sources based on $\mathrm{LiNbO_3}$ ($\sim 0.1 - 4$ THz), the quartz thickness should not exceed 130 µm. Sampling of higher THz frequencies poses limitations due to substantial dispersion of the linear THz refractive index and nonlinear susceptibility $\chi^{(2)}$ due to the 3.9, 8, 12, and 13.5 THz TO phonons of quartz [58]. This fact is especially relevant for more broadband high-field sources such as large-area spintronic emitters [5,44] and organic crystals [2,3].

The polarization sensitivity of EOS in quartz generally permits time-domain ellipsometry, allows for the direct measurement of complex and even nonequilibrium [26] tensorial material properties in anisotropic media [24,25] and optical activity of chiral phonons [27,28,59], as well as THz circular-dichroism spectroscopy [28,29], or decoding high-harmonic THz emission of complex quantum materials. The ability to detect intense THz fields in amplitude and phase without distortions is well suited for any ultrafast spectroscopy based on strong THz-field excitation [15], e.g., for understanding nonlinear THz polarization responses [40] or driving phase transitions [10–12,20], where an accurate characterization of the driving field is crucial. Moreover, the demonstrated precise helicity characterization of intense THz driving fields is urgently needed for the emerging field of chiral (or circular) phononics. In this field, lattice modes are driven on chiral or circular trajectories with phonon angular momentum [55] leading to magnetization switching [60], transient multiferroicity [23], large magnetic fields [22], or other yet unexplored spin–lattice-coupled phenomena. These first explorations in the uncharted territory of phonon-angular-momentum control highlight the challenges for THz helicity differential detection, i.e., extracting signals proportional to $S(E_{\mathrm{RCP}}) - S(E_{\mathrm{LCP}})$, which must be employed to isolate helicity-dependent effects. Using quartz as a reliable high-field THz helicity detector will help to clarify and support these novel types of measurements and will foster further studies of chiral or helicity-selective phenomena in the THz spectral region.

As the demonstrated 2D-EOS protocol only relies on a single HWP rotation, it enables a rapid measurement and, therefore, keeps the phase error from temporal drifts between adjacent EOS scans minimal. Accordingly, the scheme is also easy to implement in commercial time-domain spectrometer systems as it only relies on the addition of low-cost and widely available thin quartz wafers and standard HWPs in the VIS or NIR spectral range. As another benefit, quartz is well suited for measuring THz fields and their polarization states in systems, where space constraints often prohibit the use of motorized rotation mounts for the detection crystal, in particular in cryostats at cryogenic temperatures. Supplement 1, Fig. S5 shows quartz EOS at 80 K, demonstrating that the THz field can still be reliably sampled at low temperatures, although the response function is modified due to the enhanced phonon contribution to $\chi^{(2)}$ [16]. Conveniently, our work may also allow for all-optical synchronization of THz pump and optical probe pulses via THz slicing [61] or *in situ* field and polarization characterization in already installed z-cut quartz windows at free-electron-laser facilities, where even a noncollinear THz- and sampling-beam geometry is feasible (see Supplement 1, Fig. S2).

5. CONCLUSION

In conclusion, z-cut α-quartz can reliably sample intense THz fields of the order of 1 MV/cm without over-rotation and with negligible higher-order nonlinearities. We measured and modeled the frequency-dependent electro-optic response function, consistent with a pure bulk $\chi^{(2)}$ effect dominated by Fabry–Perot resonances, phonon modulations in the Faust–Henry formalism, phase-matching effects, and a low-frequency Debye-like contribution. We determined the electro-optic coefficient to the order of 0.1 pm/V and proved a perfect three-fold symmetry of the electro-optic response. Based on this knowledge, we developed an easily implementable protocol to measure the full vectorial THz polarization state by simply toggling between 0° and 45° sampling pulse polarizations. With this approach, we establish quartz as a powerful detector for full amplitude, phase, and polarization state of highly intense THz radiation at a fraction of the cost of conventional detection crystals. This work will accordingly foster rapid and cost-efficient high-field THz spectroscopy [7,8,15,17], THz time-domain ellipsometry [25], THz circular-dichroism spectroscopy [28,29], and will enable broadband THz helicity characterization of polarization-tailored pulses for driving angular-momentum phonons [27,28,59] or other helicity-dependent excitations [20–23] in the future.

Funding. Deutsche Forschungsgemeinschaft (469405347).

Acknowledgment. We thank A. Paarmann, Y. Behovits, A. Chekhov, and M. Wolf for fruitful discussions. S.F. Maehrlein acknowledges support and funding by the Emmy Noether Programme of the Deutsche Forschungsgemeinschaft (469405347)

Disclosures. The authors declare no conflicts of interest.

Data availability. All data needed to evaluate the conclusions in the paper are present in the paper or in the supplemental document. The experimental data and response function code are available in Ref. [62].

Supplemental document. See Supplement 1 for supporting content.

REFERENCES

1. H. Hirori, A. Doi, F. Blanchard, *et al.*, "Single-cycle terahertz pulses with amplitudes exceeding 1 MV/cm generated by optical rectification in $LiNbO_3$," Appl. Phys. Lett. **98**, 091106 (2011).
2. C. P. Hauri, C. Ruchert, C. Vicario, *et al.*, "Strong-field single-cycle THz pulses generated in an organic crystal," Appl. Phys. Lett. **99**, 161116 (2011).
3. C. Rader, Z. B. Zaccard, S.-H. E. Ho, *et al.*, "A new standard in high-field terahertz generation: the organic nonlinear optical crystal PNPA," ACS Photon. **9**, 3720–3726 (2022).
4. A. Sell, A. Leitenstorfer, and R. Huber, "Phase-locked generation and field-resolved detection of widely tunable terahertz pulses with amplitudes exceeding 100 MV/cm," Opt. Lett. **33**, 2767–2769 (2008).
5. R. Rouzegar, A. L. Chekhov, Y. Behovits, *et al.*, "Broadband spintronic terahertz source with peak electric fields exceeding 1.5 MV/cm," Phys. Rev. A **19**, 034018 (2023).
6. B. Green, S. Kovalev, V. Asgekar, *et al.*, "High-field high-repetition-rate sources for the coherent THz control of matter," Sci. Rep. **6**, 22256 (2016).
7. S. Maehrlein, A. Paarmann, M. Wolf, *et al.*, "Terahertz sum-frequency excitation of a Raman-active phonon," Phys. Rev. Lett. **119**, 127402 (2017).
8. C. L. Johnson, B. E. Knighton, and J. A. Johnson, "Distinguishing nonlinear terahertz excitation pathways with two-dimensional spectroscopy," Phys. Rev. Lett. **122**, 073901 (2019).
9. T. Kampfrath, A. Sell, G. Klatt, *et al.*, "Coherent terahertz control of antiferromagnetic spin waves," Nat. Photonics **5**, 31–34 (2010).
10. D. Fausti, R. I. Tobey, N. Dean, *et al.*, "Light-induced superconductivity in a stripe-ordered cuprate," Science **331**, 189–191 (2011).
11. X. Li, T. Qiu, J. Zhang, *et al.*, "Terahertz field-induced ferroelectricity in quantum paraelectric $SrTiO_3$," Science **364**, 1079–1082 (2019).
12. A. S. Disa, M. Curtis, A. Fechner, *et al.*, "Photo-induced high-temperature ferromagnetism in $YTiO_3$," Nature **617**, 73–78 (2023).
13. S. F. Maehrlein, I. Radu, P. Maldonado, *et al.*, "Dissecting spin-phonon equilibration in ferrimagnetic insulators by ultrafast lattice excitation," Sci. Adv. **4**, eaar5164 (2018).
14. G. Bell and M. Hilke, "Polarization effects of electro-optic sampling and over-rotation for high field THz detection," J. Infrared Millim. Terahertz Waves **41**, 880–893 (2020).
15. A. Leitenstorfer, A. S. Moskalenko, T. Kampfrath, *et al.*, "The 2023 terahertz science and technology roadmap," J. Phys. D **56**, 223001 (2023).
16. C. L. Davies, J. B. Patel, C. Q. Xia, *et al.*, "Temperature-dependent refractive index of quartz at terahertz frequencies," J. Infrared Millim. Terahertz Waves **39**, 1236–1248 (2018).
17. K. J. Tielrooij, A. Principi, D. S. Reig, *et al.*, "Milliwatt terahertz harmonic generation from topological insulator metamaterials," Light Sci. Appl. **11**, 315 (2022).
18. H. A. Hafez, S. Kovalev, J. C. Deinert, *et al.*, "Extremely efficient terahertz high-harmonic generation in graphene by hot Dirac fermions," Nature **561**, 507–511 (2018).
19. H. Chu, M. J. Kim, K. Katsumi, *et al.*, "Phase-resolved Higgs response in superconducting cuprates," Nat. Commun. **11**, 1793 (2020).
20. E. J. Sie, C. M. Nyby, C. D. Pemmaraju, *et al.*, "An ultrafast symmetry switch in a Weyl semimetal," Nature **565**, 61–66 (2019).
21. H. Ueda, M. García-Fernández, S. Agrestini, *et al.*, "Chiral phonons in quartz probed by X-rays," Nature **618**, 946–950 (2023).
22. J. Luo, T. Lin, J. Zhang, *et al.*, "Large effective magnetic fields from chiral phonons in rare-earth halides," Science **382**, 698–702 (2023).
23. M. Basini, M. Pancaldi, B. Wehinger, *et al.*, "Terahertz electric-field driven dynamical multiferroicity in $SrTiO_3$," arXiv, arXiv:2210.01690 (2022).
24. Q. Guo, Y. Zhang, Z. Lyu, *et al.*, "THz time-domain spectroscopic ellipsometry with simultaneous measurements of orthogonal polarizations," IEEE Trans. Terahertz Sci. Technol. **9**, 422–429 (2019).
25. X. Chen and E. Pickwell-MacPherson, "An introduction to terahertz time-domain spectroscopic ellipsometry," APL Photon. **7**, 071101 (2022).
26. N. Kamaraju, A. Rubano, L. Jian, *et al.*, "Subcycle control of terahertz waveform polarization using all-optically induced transient metamaterials," Light Sci. Appl. **3**, e155 (2014).
27. W. J. Choi, S. H. Lee, B. C. Park, *et al.*, "Terahertz circular Dichroism spectroscopy of molecular assemblies and nanostructures," J. Am. Chem. Soc. **144**, 22789–22804 (2022).
28. A. Baydin, F. G. Hernandez, M. Rodriguez-Vega, *et al.*, "Magnetic control of soft chiral phonons in PbTe," Phys. Rev. Lett. **128**, 075901 (2022).
29. G. Cheng, W. J. Choi, H. J. Jang, *et al.*, "Terahertz time-domain polarimetry for generalized anisotropic and chiral materials," Proc. SPIE **10917**, 1091704 (2019).
30. Z. Y. Zhang, G. Yang, F. Fan, *et al.*, "Terahertz circular dichroism sensing of living cancer cells based on microstructure sensor," Anal. Chim. Acta. **1180**, 338871 (2021).
31. A. Leitenstorfer, S. Hunsche, J. Shah, *et al.*, "Detectors and sources for ultrabroadband electro-optic sampling: experiment and theory," Appl. Phys. Lett. **74**, 1516–1518 (1999).
32. Q. Wu and X. C. Zhang, "Ultrafast electro-optic field sensors," Appl. Phys. Lett. **68**, 1604–1606 (1996).
33. Q. Wu and X. C. Zhang, "7 terahertz broadband GaP electro-optic sensor," Appl. Phys. Lett. **70**, 1784–1786 (1997).
34. T. Kampfrath, J. Nötzold, and M. Wolf, "Sampling of broadband terahertz pulses with thick electro-optic crystals," Appl. Phys. Lett. **90**, 231113 (2007).
35. L. Huber, S. F. Maehrlein, F. Wang, *et al.*, "The ultrafast Kerr effect in anisotropic and dispersive media," J. Chem. Phys. **154**, 094202 (2021).
36. R. X. Zhang, Y. Cui, W. Sun, *et al.*, "Polarization information for terahertz imaging," Appl. Opt. **47**, 6422–6427 (2008).
37. N. Nemoto, T. Higuchi, N. Kanda, *et al.*, "Highly precise and accurate terahertz polarization measurements based on electro-optic sampling with polarization modulation of probe pulses," Opt. Express **22**, 17915–17929 (2014).
38. N. C. J. van der Valk, W. A. van der Marel, and P. C. Planken, "Terahertz polarization imaging," Opt. Lett. **30**, 2802–2804 (2005).
39. M. Cornet, J. Degert, E. Abraham, *et al.*, "Terahertz Kerr effect in gallium phosphide crystal," J. Opt. Soc. Am. B **31**, 1648–1652 (2014).
40. M. Frenzel, M. Cherasse, J. M. Urban, *et al.*, "Nonlinear terahertz control of the lead halide perovskite lattice," Sci. Adv. **9**, eadg3856 (2023).
41. K. J. Kaltenecker, E. J. Kelleher, B. Zhou, *et al.*, "Attenuation of THz beams: a "how to" tutorial," J. Infrared Millim. Terahertz Waves **40**, 878–904 (2019).
42. S. Zibod, P. Rasekh, M. Yildrim, *et al.*, "Strong nonlinear response in crystalline quartz at THz frequencies," Adv. Opt. Mater. **11**, 2202343 (2023).
43. Y. X. Wei, J. Le, L. Huang, *et al.*, "Efficient generation of intense broadband terahertz pulses from quartz," Appl. Phys. Lett. **122**, 081105 (2023).
44. V. Balos, M. Wolf, S. Kovalev, *et al.*, "Optical rectification and electro-optic sampling in quartz," Opt. Express **31**, 13317–13327 (2023).
45. J. Shan, J. I. Dadap, and T. F. Heinz, "Circularly polarized light in the single-cycle limit: the nature of highly polychromatic radiation of defined polarization," Opt. Express **17**, 7431–7439 (2009).
46. G. Ghosh, "Dispersion-equation coefficients for the refractive index and birefringence of calcite and quartz crystals," Opt. Commun. **163**, 95–102 (1999).

47. W. L. Faust and C. H. Henry, "Mixing of visible and near-resonance infrared light in GaP," Phys. Rev. Lett. **17**, 1265–1268 (1966).
48. D. D. Eden and G. H. Thiess, "Measurement of the direct electro-optic effect in quartz at UHF," Appl. Opt. **2**, 868–869 (1963).
49. R. D. Rosner, E. H. Turner, and I. P. Kaminow, "Clamped electrooptic coefficients of KDP and quartz," Appl. Opt. **6**, 778 (1967).
50. M. Thämer, T. Garling, R. K. Campen, *et al.*, "Quantitative determination of the nonlinear bulk and surface response from alpha-quartz using phase sensitive SFG spectroscopy," J. Chem. Phys. **151**, 064707 (2019).
51. F. Terki, C. Levelut, M. Boissier, *et al.*, "Low-frequency dynamics and medium-range order in vitreous silica," Phys. Rev. B **53**, 2411–2418 (1996).
52. U. Buchenau, N. Nücker, and A. J. Dianoux, "Neutron scattering study of the low-frequency vibrations in vitreous silica," Phys. Rev. Lett. **53**, 2316–2319 (1984).
53. M. Naftaly and A. Gregory, "Terahertz and microwave optical properties of single-crystal quartz and vitreous silica and the behavior of the boson peak," Appl. Sci. **11**, 6733 (2021).
54. R. W. Boyd, *Nonlinear Optics*, 3rd ed. (Academic, 2008).
55. S. R. Tauchert, M. Volkov, D. Ehberger, *et al.*, "Polarized phonons carry angular momentum in ultrafast demagnetization," Nature **602**, 73–77 (2022).
56. E. Castro-Camus and M. B. Johnston, "Extraction of the anisotropic dielectric properties of materials from polarization-resolved terahertz time-domain spectra," J. Opt. A: Pure Appl. Opt. **11**, 105206 (2009).
57. C. Chou, Y. C. Huang, and M. Chang, "Precise optical activity measurement of quartz plate by using a true phase-sensitive technique," Appl. Opt. **36**, 3604–3609 (1997).
58. K. D. Cummings and D. B. Tanner, "Far-infrared ordinary-ray optical-constants of quartz," J. Opt. Soc. Am. **70**, 123–126 (1980).
59. W. J. Choi, K. Yano, M. Cha, *et al.*, "Chiral phonons in microcrystals and nanofibrils of biomolecules," Nat. Photonics **16**, 366–373 (2022).
60. C. S. Davies, F. G. N. Fennema, A. Tsukamoto, *et al.*, "Phononic switching of magnetization by the ultrafast Barnett effect," arXiv, arXiv:2305.11551 (2023).
61. M. Chen, T. V. A. G. de Oliveira, I. Ilyakov, *et al.*, "Terahertz-slicing-an all-optical synchronization for 4th generation light sources," Opt. Express **30**, 26955–26966 (2022).
62. M. Frenzel, J. M. Urban, L. Nest, *et al.* "Quartz as an accurate high-field low-cost THz helicity detector - data sets and code," Zenodo (2024), https://doi.org/10.5281/zenodo.10569258.